A Methodology to Relate Black Carbon Particle Number and Mass Emissions

Roger Teoh[1], Marc E.J. Stettler[1]*, Arnab Majumdar[1], Ulrich Schumann[2], Brian Graves[3] and Adam Boies[3]

[1] Centre for Transport Studies, Department of Civil and Environmental Engineering, Imperial College London, London, SW7 2AZ, United Kingdom

[2] Deutsches Zentrum für Luft- und Raumfahrt, Institute of Atmospheric Physics, 82234 Oberpfaffenhofen, Germany

[3] Department of Engineering, University of Cambridge, Cambridge, CB2 1PZ, United Kingdom

* Corresponding author. E-mail address: m.stettler@imperial.ac.uk

Abstract

Black carbon (BC) particle number (PN) emissions from various sources contribute to the deterioration of air quality, adverse health effects, and anthropogenic climate change. This paper critically reviews different fractal aggregate theories to develop a new methodology that relates BC PN and mass concentrations (or emissions factors). The new methodology, named as the fractal aggregate (FA) model is validated with measurements from three different BC emission sources: an internal combustion engine, a soot generator, and two aircraft gas turbine engines at ground and cruise conditions. Validation results of the FA model show that R^2 values range from 0.44 to 0.95, while the Normalised Mean Bias is between -27.7% and +26.6%. The model estimates for aircraft gas turbines represent a significant improvement compared to previous methodologies used to estimate aviation BC PN emissions, which relied on simplified assumptions. Uncertainty and sensitivity analyses show that the FA model estimates have an asymmetrical uncertainty bound $(-54\%, +103\%)$ at a 95% confidence interval for aircraft gas turbine engines and are most sensitive to uncertainties in the geometric standard deviation of the BC particle size distribution. Given the improved performance in estimating BC PN emissions from various sources, we recommend the implementation of the FA model in future health and climate assessments, where the impacts of PN are significant.

Keywords: Black carbon; Particle number; Particle Mass; Fractal aggregates; Combustion emissions.

Nomenclature

BC	Black Carbon
C	Mass-mobility prefactor
C_{ov}	Coefficient on the degree of primary particle overlapping in a BC aggregate
CIDI	Compression-Ignition natural gas Direct-Injection engine
CPC	Condensation Particle Counter
CPMA	Centrifugal Particle Mass Analyzer
d_{m}	Mobility diameter (m, unless stated otherwise)
d_{pp}	Primary particle diameter (m, unless stated otherwise)
D_{α}	Projected area exponent
D_{fm}	Mass mobility exponent
D_{TEM}	Transmission Electron Microscopy exponent
DAC	Double Annular Combustor
DLCA	Diffusion Limited Cluster Aggregation
DMA	Differential Mobility Analyzer
EI_{m}	Mass Emissions Index (g kg^{-1})
EI_{n}	Number Emissions Index (kg^{-1})
F_{00}	Maximum rated thrust at sea level static conditions (N)
F/F_{00}	Aircraft engine thrust setting as a percentage of F_{00}
FA	Fractal Aggregates
GDI	Gasoline Direct Injection engine
GMD	Geometric Mean Diameter (m, unless stated otherwise)
GSD	Geometric Standard Deviation
HPDI	High Pressure Direct Injection
ICAO	International Civil Aviation Organization
IPSD	Integrated Particle Size Distribution Method
k	Density-mobility prefactor
k_{a}	Scaling prefactor
k_{fm}	Mass-mobility prefactor
k_{TEM}	Transmission Electron Microscopy prefactor
Kn	Knudsen Number
LII	Laser Induced Incandescence
m	Mass of one black carbon aggregate (kg)
M	Total mass (or concentration) of black carbon aggregates in a particle size distribution (kg or kg m^{-3})
n_{pp}	Number of primary particles in a black carbon aggregate
N	Total number (or concentration) of black carbon aggregates in a particle size distribution (1, or m^{-3})
NMB	Normalised Mean Bias
nvPM	non-volatile Particulate Matter
PM	Particulate Matter
PMP	Particle Measurement Programme
PN	Particle Number
PSAP	Particle Soot Absorption Photometer
PSD	Particle Size Distribution
R^2	Coefficient of determination

RLCA Reaction-Limited Cluster Aggregation
SAC Single Annular Combustor
SI Supporting Information
SMPS Scanning Mobility Particle Sizer
TEM Transmission Electron Microscopy
UNECE United Nations Economic Commission for Europe
ρ_0 Material density of black carbon (= 1770 kg m^{-3})
ρ_{eff} Effective density of black carbon (kg m^{-3})

1 Introduction

Black carbon (BC) particles are carbonaceous aerosols that have a high thermal stability, strong light-absorbing properties and are generally resistant to chemical transformation (Goldberg, 1985; Petzold et al., 2013). These carbonaceous aerosols are aggregates that consist of smaller spherical primary particles and exhibit ‘fractal-like’ properties due to their self-similar structure over a finite length scale (Sorensen, 2011). BC aggregates are mainly formed in flames due to the incomplete combustion of biomass and fossil fuels, and these emissions contribute to anthropogenic climate change, the deterioration of air quality and adverse human health (Bond et al., 2013; Penner et al., 1999).

The transport sector is a major source of BC emissions. Combustion engines emit a mixture of particulate matter (PM) often called ‘soot’ including solid particles (such as BC and metallic compounds) and organic (volatile) particles (Abegglen et al., 2015; Petzold et al., 2013; UNECE, 2010). BC typically accounts for around 75% of the total solid particle mass (Kittelson, 1998), while the fraction of organic content to total carbon emitted in engine exhausts generally range from 5% to 85% and decreases as engine power increases (Anderson et al., 2011; Delhaye et al., 2017; Graves et al., 2015; Wey et al., 2006).

At a macroscopic level, BC is commonly quantified in terms of its mass and number concentration. For emission sources, the mass and number emission rates are most commonly quantified in terms of the emitted BC per distance travelled (g/km, or km^{-1}), per unit energy (g (kWh)$^{-1}$, or kWh^{-1}), per unit time (g s^{-1}, or s^{-1}), or as an emissions index per mass of fuel burned (EI_m in g kg^{-1}, or EI_n in kg^{-1}). Measurements show that BC number and mass concentrations in the exhaust of internal combustion engines ranges from 10^{12} to 10^{14} m^{-3}, and 0.1 to 30 mg m^{-3} respectively for different engines and operating conditions (Abdul-Khalek et al., 1998; Brian Graves et al., 2015).

To address the emissions of solid particle number (PN) from motorised vehicles, the results of the particle measurement programme (PMP), a working group established by the United Nations Economic Commission for Europe (UNECE) was integrated into the Euro 5/V and 6/VI emissions standards, which limit the solid PN emissions from light and heavy-duty vehicles to 6×10^{11} km^{-1} and 8×10^{11} kWh^{-1} respectively (Giechaskiel et al., 2014; Martini et al., 2009). Prior to the PMP, measurements of solid particle mass concentrations were more commonly available than PN concentrations because pre-Euro 5/V emission standards only specified a limit on the mass emissions (Burtscher, 2005).

However, due to the increasing evidence that existing mass-based metrics are inadequate in characterising the negative health effects of air pollution, particle number and surface area concentration are being proposed as additional metrics for air quality assessments (Janssen et al., 2011; Peters et al., 2011). Recent health studies have shown that condensed compounds of semi-volatile chemicals of high toxicity could adsorb on the surfaces of ultrafine particles (Schmid & Stoeger, 2016; Steiner et al., 2016). Given that ultrafine particles have a higher probability of being deposited to the respiratory epithelium, translocated towards the circulatory system and accumulate in various organs (Kreyling et al., 2006), a prolonged exposure to these elevated concentrations of BC can subsequently increase the risk of cardiopulmonary disease and premature mortality (Laden et al., 2006; Pope III & Dockery, 2006).

For aircraft emissions at cruise altitudes, BC particles can have a longer atmospheric lifetime ($\approx$ 4 to 30 days) (Bond et al., 2013; Williams et al., 2002) relative to ground level sources ($\approx$ 4 to 7 days) (Samset et al., 2014; Wang, 2004) because of the absence of an efficient wet scavenging removal process in the stratosphere (Barrett et al., 2010a). These aerosols also interact with the formation, lifetime and albedo of cirrus clouds (Boucher, 2011). Studies using global cloud-aerosol climate models have shown that the indirect climate forcing of aircraft BC ($\approx$ 0.01 W m^{-2} to 0.09 W m^{-2}) may outweigh its direct forcing ($\approx$ 0.0034 W m^{-2} to 0.02 W m^{-2}), though these estimates are highly sensitive to assumptions regarding the number and size of BC particles (Brasseur et al., 2016; Lee et al., 2010; Stettler et al., 2013a; Zhou & Penner, 2014). Under ice super-saturated conditions however, BC PN emissions from an aircraft strongly influence different contrail properties and their subsequent climate impact (Burkhardt et al., 2018; Jeßberger et al., 2013; Kärcher & Yu, 2009).

Although the BC EI_n is an essential input parameter for contrail models (Caiazzo et al., 2017; Schumann, 2012), existing models rely on simplified assumptions leading to large uncertainty bounds of up to one order of magnitude (Anderson et al., 2011). For example, Petzold et al. (1999) and Caiazzo et al. (2017) estimated EI_n by dividing the total BC mass emission with a constant BC particle mass; Döpelheuer (2002) developed an EI_n/EI_m ratio with a dependence on flight altitude; and finally Barrett et al. (2010b) estimated EI_n by assuming a log-normal distribution with a fixed geometric mean diameter (GMD) and geometric standard deviation (GSD) value. Numerous studies have subsequently shown that the properties and size distribution of BC emitted from aircraft engines are highly dependent on engine thrust settings (Abegglen et al., 2015; Boies et al., 2015; Delhaye et al., 2017; Durdina et al., 2014; Johnson et al., 2015; Lobo et al., 2015a; Peck et al., 2013), where the GMD of aircraft emitted BC typically range from 10 nm to 50 nm, while the GSD varies from 1.4 to 1.9 (Durdina et al., 2014; Lobo et al., 2015b).

A new non-volatile particulate matter (nvPM) measurement procedure is currently being developed by the International Civil Aviation Organization (ICAO), however it will only be applied to new aircraft engines with a rated thrust above 26.7 kN after January 2020 (ICAO, 2016). Given that there is currently no proposal to retroactively measure BC emission characteristics from existing certified turbofan engines and the limitations of existing aircraft EI_n models, a reliable and improved method by which to estimate aircraft BC EI_n is needed.

This paper therefore aims to: (i) develop a new model to estimate BC PN emissions from mass measurements or estimates using the theory of fractal aggregates; (ii) validate the new model using measurements of BC from three different emission sources (an internal combustion engine, a soot generator, and two aircraft gas turbine engines); and (iii) quantify the uncertainty bound and conduct a sensitivity analysis for the new model.

Section 2 outlines the theory used in the development of the new methodology to relate BC PN and mass emissions. Section 3 describes the materials and methods used to validate the new model. Section 4 presents the validation results and Section 5 conducts an uncertainty and sensitivity analysis for this new model. Finally, Section 6 concludes and summarises the key findings from this paper. Details and data omitted from the main text are included in the Supporting Information (SI) as referenced.

2 Theoretical development

This section reviews the different fractal aggregate theories that describe aggregate properties including mass, diameter and morphology. We then develop a new model to relate the total mass and number of a population of polydisperse aggregates, which accounts for the particle size distribution (PSD) and aggregate morphology. The model is subsequently applied to estimate BC PN concentration (or emissions factor) from mass concentration (or emissions factor) for various emission sources in Section 4.

2.1 Existing theories to estimate BC aggregate mass

Four equations are commonly used to estimate the mass of one BC aggregate (m) with varying assumptions. Firstly, m can be fundamentally represented as the summation of individual primary particle masses (Boies et al., 2015; Eggersdorfer et al., 2012b),

$$m = n_{\mathrm{pp}}\rho_0(\frac{\pi}{6})d_{\mathrm{pp}}{}^3 , \tag{1}$$

where n_{pp} is the number of primary particles in an aggregate, d_{pp} is the BC primary particle diameter, and ρ_0 is the BC material density. ρ_0 is reported to be in a range of between 1820 kg m^{-3} and 2050 kg m^{-3} (Dobbins et al., 1994), while a more recent study on diesel soot agglomerates estimated ρ_0 to be around 1770 ± 70 kg m^{-3} (Park et al., 2004). In Eq. 1, pairs of primary particles in an aggregate are assumed to have a non-overlapping single point of contact. However, several studies have shown some degree of overlapping between pairs of primary particles (Bourrous et al., 2018; Brasil et al., 1999; Moran et al., 2018; Wentzel et al., 2003), and the partial overlapping between primary particles can be defined with an overlapping coefficient,

$$\mathrm{C_{ov}} = \frac{(r_{\mathrm{i}}+r_j)-d_{\mathrm{ij}}}{(r_{\mathrm{i}}+r_{\mathrm{j}})}, \tag{2}$$

where r_i and r_j are the radiuses of primary particles i and j, and d_{ij} is the length between the centres of both primary particles. C_{ov} values are estimated from transmission electron microscopy (TEM) observations or numerical simulations, and typically range from 0.05 to 0.25 for aggregates with monodisperse and polydisperse primary particles (Bourrous et al., 2018; Brasil et al., 1999; Moran et al., 2018; Wentzel et al., 2003). For aggregates with monodisperse and overlapping primary particles, Moran et al. (2018) shows that m decreases as a cubic function of C_{ov},

$$m = n_{\mathrm{pp}}\rho_0\left(\frac{\pi}{6}\right)d_{\mathrm{pp}}{}^3\left[n_{pp} - \left(n_{pp} - 1\right)\left(\frac{1}{2}\right)(3 - C_{ov})C_{ov}{}^2\right] \tag{3}$$

More commonly, measurements of *m* and aggregate mobility diameter (d_{m}) are often linked by a power-law relationship (Abegglen et al., 2015; Dastanpour et al., 2017; Johnson et al., 2015),

$$m = C d_{\mathrm{m}}{}^{D_{\mathrm{fm}}}\ , \tag{4}$$

where *C* is the mass-mobility prefactor with units of kg $\mathrm{m}^{-D_{\mathrm{fm}}}$. D_{fm} is the mass-mobility exponent, used to describe the morphology of BC aggregates (DeCarlo et al., 2004) and has a theoretical interval from 1.0 for long-chains to 3.0 for spherical aggregates (Durdina et al., 2014). BC aggregates emitted by various sources typically have a D_{fm} in the range of 1.8 to 2.8 (Abegglen et al., 2015; Dastanpour et al., 2017; Graves et al., 2015; Johnson et al., 2015).

Finally, the d_{pp} can also be included in a power-law relating *m* to d_{m} and d_{pp} (Eggersdorfer et al., 2012b; Park, Kittelson, & McMurry, 2004),

$$m = k_{\mathrm{fm}}\left(\frac{d_{\mathrm{m}}}{d_{\mathrm{pp}}}\right)^{D_{\mathrm{fm}}}, \tag{5}$$

where k_{fm} is also named as the mass-mobility prefactor with metric units of mass (kg). Note, the prefactors *C* and k_{fm} have different units and are therefore not equivalent.

The power-law mass-mobility relationships of Eq. 4 and 5 can be used to quantify the effective density of a BC aggregate (ρ_{eff}) (McMurry et al., 2002),

$$m = \rho_{\mathrm{eff}}\left(\frac{\pi}{6}\right)d_{\mathrm{m}}{}^3. \tag{6}$$

ρ_{eff} is the density of the fractal aggregate when its volume is taken to be that of its mobility-equivalent sphere. While the value of ρ_0 is constant for all conditions, ρ_{eff} typically decreases as d_{m} increases (Abegglen et al., 2015; Johnson et al., 2015) due to BC aggregates having more open space as d_{m} increases (Graves et al., 2015).

With experimental measurements of *m*, Eq. 4 can be equated with Eq. 4 or 5 to estimate ρ_{eff} for a given d_{m},

$$\rho_{\mathrm{eff}} = \frac{m}{\left(\frac{\pi}{6}\right)d_{\mathrm{m}}{}^3} = k d_m{}^{(D_{fm}-3)}\ . \tag{7}$$

The density-mobility prefactor *k* has the same units as *C* (kg $\mathrm{m}^{-D_{\mathrm{fm}}}$) and is related to the mass-mobility prefactors *C* ($k = \frac{6C}{\pi}$, Eq. 4) and k_{fm} ($k = \frac{6k_{\mathrm{fm}}}{\pi {d_{\mathrm{pp}}}^{D_{\mathrm{fm}}}}$, Eq. 5). Experimentally, the average *m* and ρ_{eff} as a function of d_{m} are commonly determined using a differential mobility analyser (DMA), aerosol particle mass (APM) or centrifugal particle mass analyzer (CPMA) and condensation particle counter (CPC) set up (Johnson et al., 2013). ρ_{eff} is also commonly used to estimate total mass of BC aggregates (*M*) from the total number of BC aggregates in a PSD (*N*), as will be described in Section 3.1.

2.2 Number of primary particles in an aggregate

The Knudsen number (Kn) is a dimensionless number defined as the ratio of the molecular mean free path to the particle radius. Sorensen (2011) showed that BC aggregates are formed via the diffusion limited cluster aggregation (DLCA) process in the free molecular flow regime where the mean free path is greater than the particle radius (Kn ≥ 1). An example of a condition which sees Kn ≥ 1 includes low-density gas flows, where the continuum assumption becomes invalid due to the minimal interaction between molecules (Hinds, 1999).

In the free molecular and transition regimes, n_{pp} can be related to d_{m} and d_{pp} (Boies et al., 2015; Eggersdorfer et al., 2012a),

$$n_{\mathrm{pp}} = k_{\mathrm{a}}\left(\frac{d_{\mathrm{m}}}{d_{\mathrm{pp}}}\right)^{2D_{\alpha}} , \tag{8}$$

where k_{a} and D_{α} are the scaling prefactor and projected area exponent, respectively. The values of k_{a} and D_{α} are calibrated from experimental measurements or numerical simulations (Dastanpour et al., 2016). By equating Eq. 1 with Eq. 4, or Eq. 1 with Eq. 5, it can be shown that $2D_{\alpha} = D_{\mathrm{fm}}$ (Eggersdorfer et al., 2012b), while k_{a} can also be derived from empirical values of *C* and k_{fm},

$$k_{\mathrm{a}} = \frac{6C}{\rho_0 \pi} {d_{\mathrm{pp}}}^{(D_{\mathrm{fm}}-3)} \text{ (from Eq. 1 \& 4)} \quad \text{or} \quad k_{\mathrm{a}} = \frac{k_{fm}}{\rho_0 \pi {d_{pp}}^3} \text{ (from Eq. 1 \& 5)} \tag{9}$$

where an average primary particle diameter d_{pp} is taken from TEM observations. For aggregates formed via DLCA, Eggersdorfer & Pratsinis (2012) showed that k_{a} is inversely proportional to the GSD of primary particle diameters. Therefore, k_{a} can be used to infer the polydispersity of primary particle sizes in an aggregate. We also evaluated the validity of $2D_{\alpha} = D_{\mathrm{fm}}$ by comparing the datasets of Boies et al. (2015) and Johnson et al. (2015), with an average difference of 25% between $2D_\alpha$ and D_{fm} (shown in SI.2). This discrepancy could be due to the different calibration methods used to obtain values of D_{fm} (estimated using mass-mobility data) and D_α (estimated using TEM and mass-mobility data).

With constant values of k_a = 0.998 and D_α = 1.069, Eggersdorfer et al. (2012b) showed that Eq. 8 is valid for aggregates formed of polydisperse primary particles, irrespective of the sintering mechanism or the state of sintering. Using experimental data from a compression-ignition natural-gas direct-injection (CIDI) engine, Dastanpour et al. (2016) evaluated the validity of the constant k_a and D_α values (Eggersdorfer et al., 2012b) by comparing it with fitted k_a and D_α values for specific operating conditions. With the constant and fitted values of k_a and D_α, d_{pp} is estimated using Eq. 8 and compared with analysis of TEM images. The results of Dastanpour et al. (2016) suggest that errors of d_{pp} can be reduced by 30% when fitted k_a and D_α values are used instead of the constant k_a and D_α values from Eggersdorfer et al. (2012b). Further assessments regarding the assumptions of k_a = 0.998 and D_α = 1.069 will be discussed in Section 4.

2.3 Relationship between primary particle and aggregate mobility diameter

For both diesel internal combustion engines and aircraft gas turbines, d_{pp} ranges from 13 to 26 nm over different engine operating conditions (Graves et al., 2015; Liati et al., 2014). Studies have indicated that d_{pp} is correlated with the aggregate diameter: Boies et al. (2015) showed that d_{pp} is related to d_m, whilst Dastanpour & Rogak (2014) related d_{pp} to the projected area equivalent diameter (d_a). Given that d_m is approximately equal to d_a in the free molecular and transition regime (Dastanpour et al., 2016; Eggersdorfer et al., 2012b; Rogak et al., 1993), this relationship can be generalised as,

$$d_{pp} = k_{TEM} {d_m}^{D_{TEM}} , \qquad (10)$$

where d_{pp} is the arithmetic mean of the primary particle diameters within an aggregate, while k_{TEM} and D_{TEM} are fitted parameters. The observed correlation between d_{pp} and d_m or d_a is likely due to the “external mixing hypothesis” (Rogak & Olfert, 2019), where primary particles and aggregates form and coalesce in heterogeneous regions in the combustion chamber with different local equivalence ratios and temperatures. The BC aggregates formed in the different regions of the combustion chamber are then externally mixed to form the ensemble of aggregates measured in the exhaust. Therefore, the relative variations of the primary particle diameters within individual aggregates (or the GSD of primary particles) are typically much smaller than the ensemble of aggregates (Dastanpour & Rogak, 2014; Dastanpour et al., 2016; Rogak & Olfert, 2019), which also mean that the difference between different averages used for the d_{pp} (i.e. average mass, arithmetic mean or median) is likely to be small (Rogak, 2019).

Table 1 shows the typical k_{TEM} and D_{TEM} coefficient values for various BC emission sources (Boies et al., 2015; Dastanpour & Rogak, 2014). We note that the difference between averages used for the d_{pp} may affect these k_{TEM} and D_{TEM} coefficients, but that difference is likely to be within the 95% confidence interval stated in Dastanpour & Rogak (2014), and in the SI.9.1 (Rogak, 2019).

Table 1: k_{TEM} and D_{TEM} coefficient values for Eq. 10 for various BC emission sources. The coefficient values of k_{TEM} and D_{TEM} are valid for d_{m} and d_{pp} in metres.

Emission Source	Coefficients, $d_{\mathrm{pp}}[\mathrm{m}] = k_{\mathrm{TEM}} \times d_{\mathrm{m}}{}^{D_{\mathrm{TEM}}}$		Ref.
	k_{TEM}	D_{TEM}	
Gasoline Direct Injection engine (GDI)	2.616×10^{-6}	0.30	[1]
High Pressure Direct Injection (HPDI)	2.644×10^{-6}	0.29	
Inverted burner	2.465×10^{-6}	0.29	
Aircraft gas turbine engine	1.621×10^{-5}	0.39	
Aircraft gas turbine engine	0.0125	0.8	[2]

[1] Dastanpour & Rogak (2014) [2] Boies et al. (2015)

2.4 Relating mass and number of polydisperse fractal aggregates

Table 2 provides a summary of the equations that are available to relate different fractal aggregate properties. For the equations that were fitted with a power-law relationship, five distinct prefactor-exponent coefficient pairs are identified and compiled. The equations listed in Table 2 will be assessed and selected to develop a new model to relate BC PN emissions and mass.

Table 2: Summary of equations used to relate different fractal aggregate properties. Specific references are denoted by square brackets.

Eqn.		Coefficient Pairs	Formula	Remarks	Reference
BC Aggregate Mass (m)	1	-	$m = n_{\mathrm{pp}}\rho_0(\frac{\pi}{6})d_{\mathrm{pp}}{}^3$	m is calculated by multiplying the material density of BC (ρ_0) with the volume of each primary particles. Single point of contact is assumed between pairs of primary particles.	[2], [9]
	3	-	$m = n_{\mathrm{pp}}\rho_0\left(\frac{\pi}{6}\right)d_{\mathrm{pp}}{}^3\left[n_{pp} - (n_{pp}-1)\left(\frac{1}{2}\right)(3 - C_{ov})C_{ov}{}^2\right]$	Similar to Eq. 1, but partial overlapping between primary particles is accounted by C_{ov}. C_{ov} estimated from TEM observations or numerical simulation and typically ranges from 0.05 to 0.25. m decreases as a cubic function of C_{ov}	[3], [4], [14], [16]
	4	(C, D_{fm})	$m = Cd_{\mathrm{m}}{}^{D_{\mathrm{fm}}}$	C and D_{fm} are empirically calibrated from measurements of m & d_m. d_{pp} data not required for calibration. C ranges from 10^{-5} to 15. D_{fm} ranges from 1.8 to 2.8.	[1], [6], [11], [12]
	5	(k_{fm}, D_{fm})	$m = k_{\mathrm{fm}}(\frac{d_{\mathrm{m}}}{d_{\mathrm{pp}}})^{D_{\mathrm{fm}}}$	k_{fm} and D_{fm} are empirically calibrated from measurements of m, d_m & d_{pp}.	[8], [9], [15]
	6 & 7	(k, D_{fm})	$m = \rho_{\mathrm{eff}}(\frac{\pi}{6})d_{\mathrm{m}}{}^3$ $\downarrow$ $\rho_{\mathrm{eff}} = kd_m{}^{(D_{fm}-3)}$	k is a derived quantity, estimated from C (Eq. 4) or k_{fm} (Eq. 5). k is inversely proportional to D_{fm}. k ranges from 10^{-2} to 35.	[1], [6], [11], [12], [13]
No. of primary particles in an aggregate (n_{pp})	8 & 9	(k_a, D_α)	$n_{\mathrm{pp}} = k_{\mathrm{a}}(\frac{d_{\mathrm{m}}}{d_{\mathrm{pp}}})^{2D_\alpha}$	k_a and D_α can be empirically calibrated from measurements of n_{pp}, d_m & d_{pp}. k_a can be derived using data from the prefactor. C (Eq. 4) or k_{fm} (Eq. 5), and the average d_{pp} of BC aggregates. Theoretically, $D_{fm} = 2D_\alpha$. k_a and D_α decreases as GSD of d_{pp} increases. k_a and D_α for DLCA ranges from 0.6 to 1.1, and 0.8 to 1.1 respectively.	[2], [8], [9], [10]
Primary Particle Diameter (d_{pp})	10	(k_{TEM}, D_{TEM})	$d_{\mathrm{pp}} = k_{\mathrm{TEM}}d_{\mathrm{m}}{}^{D_{\mathrm{TEM}}}$	k_{TEM} and D_{TEM} can be empirically calibrated from measurements of d_m and d_{pp}. k_{TEM} ranges from 10^{-6} to 10^{-2}. D_{TEM} ranges from 0.3 to 1.0.	[2], [5], [6], [7]

[1] Abegglen at al. (2015)
[2] Boies et al. (2015)
[3] Bourrous et al. (2018)
[4] Brasil et al. (1999)
[5] Dastanpour et al. (2016)
[6] Dastanpour et al. (2017)
[7] Dastanpour & Rogak (2014)
[8] Eggersdorfer et al. (2012a)
[9] Eggersdorfer et al. (2012b)
[10] Eggersdorfer & Pratsinis (2012)
[11] Graves et al. (2015)
[12] Johnson et al. (2015)
[13] McMurry et al. (2002)
[14] Moran et al. (2018)
[15] Park et al. (2004)
[16] Wentzel et al. (2003)

Eq. 1 and Eq. 3 fundamentally relate the mass of agglomerates (single point contact) and aggregates (sintered and overlapping) to the sum of the mass of BC primary particles respectively, without reliance on a prefactor-exponent coefficient pair. First, we use Eq. 1 as the foundation for the new BC PN-mass model. Then in Section 2.5 we show the model accounting for overlapping of primary particles derived from Eq. 3.

By substituting the n_{pp} and d_{pp} expressions from Eq. 8 and Eq. 10 into Eq. 1, m can be estimated as a function of d_m,

$$m = k_{\mathrm{a}} {d_{\mathrm{m}}}^{\varphi} \rho_0 (\frac{\pi}{6}) (k_{\mathrm{TEM}})^{(3-2D_\alpha)}, \tag{11}$$

where $\varphi = 3D_{\mathrm{TEM}} + (1 - D_{\mathrm{TEM}})2D_\alpha$.

The total mass of aggregates (M) in a PSD can then be calculated using the integrated product of the aggregate mass and number weighted distribution, $n(d_{\mathrm{m}}) = \frac{\mathrm{d}N}{\mathrm{dlog}d_{\mathrm{m}}}$, with $\int_0^\infty n(d_{\mathrm{m}})\, \mathrm{dlog}d_{\mathrm{m}} = N$ is the total number of aggregates,

$$M = \int_0^\infty m(d_{\mathrm{m}}) n(d_{\mathrm{m}})\, d\mathrm{log}d_{\mathrm{m}}\ , \tag{12}$$

The relationship linking each BC aggregate mass to its mobility diameter, $m(d_m)$ from Eq. 11 is substituted into Eq. 12,

$$M = N k_a \rho_0 (\frac{\pi}{6}) (k_{TEM})^{3-2D_\alpha} \int_0^\infty {d_{\mathrm{m}}}^{\varphi}\, d\mathrm{log}d_{\mathrm{m}}\ . \tag{13}$$

If the PSD is assumed to be a mono-modal lognormal distribution defined by GMD and GSD, the remaining integral in Eq. 13 is equal to the φ^{th} moment of a log-normal distribution,

$$M = N k_a \rho_0 (\frac{\pi}{6}) (k_{TEM})^{3-2D_\alpha} \mathrm{GMD}^{\varphi} \exp(\frac{\varphi^2 \ln(\mathrm{GSD})^2}{2})\ . \tag{14}$$

Eq. 14 can then be rearranged to give N,

$$N = \frac{M}{k_{\mathrm{a}} \rho_0 (\frac{\pi}{6}) (k_{\mathrm{TEM}})^{3-2D_\alpha} \mathrm{GMD}^{\varphi} \exp(\frac{\varphi^2 \ln(\mathrm{GSD})^2}{2})}, \tag{15}$$

where $\varphi = 3D_{\mathrm{TEM}} + (1 - D_{\mathrm{TEM}})2D_\alpha$.

The variables M and N can be used interchangeably with the concentration of BC mass (kg m^{-3}) and number (m^{-3}), emission indices BC EI_m (g kg^{-1}) and EI_n (kg^{-1}), or their respective emissions factors. Eq. 15, named as the Fractal Aggregates (FA) model represents a relationship between number and mass of fractal aggregates, and also accounting for the BC PSD and morphology. The derivation of the FA model can be found in SI.1.1

2.5 Accounting for Primary Particle Overlapping in the FA Model

When primary particle overlapping is included to estimate m using Eq. 3 in place of Eq. 1, the FA model becomes:

$$N = \frac{M}{\rho_0 \left(\frac{\pi}{6}\right) [k_{\mathrm{a}}(k_{\mathrm{TEM}})^{3-2D_\alpha} \mathrm{GMD}^{\varphi} \exp\left(\frac{\varphi^2 \ln(\mathrm{GSD})^2}{2}\right)(1 - 1.5C_{ov}^2 + 0.5C_{ov}^3) + k_{TEM}^3 (\frac{1}{2})(1.5C_{ov}^2 - 0.5C_{ov}^3)\mathrm{GMD}^{\gamma} \exp\left(\frac{\gamma^2 \ln(\mathrm{GSD})^2}{2}\right)]}$$

$$\text{where } \varphi = 3D_{\mathrm{TEM}} + (1 - D_{\mathrm{TEM}})2D_\alpha \quad \& \quad \gamma = 3D_{\mathrm{TEM}}. \tag{16}$$

This equation reverts to Eq. 15 when $C_{ov} = 0$. The extended derivation of the FA model (Eq. 16) is shown in SI.1.2. Although this form of the FA model is more complete, we note that there is limited quantification of C_{ov} for different BC emission sources. Previous studies have predominantly used numerical simulations to estimate C_{ov} for different nanoparticles (Brasil et al., 1999; Moran et al., 2018). Bourrous et al. (2018) and Wentzel et al. (2003) used TEM images to quantify the C_{ov} for different nanoparticles as being in the range of 0.02 to 0.24, however, there remains limited information on the variation of C_{ov} on combustion conditions.

We note that the ratio between N estimated with the effects of overlapping (Eq. 16) is up to 7% higher than when overlapping is neglected (Eq. 15) for an upper bound of $C_{ov} = 0.24$ for BC aggregates (Bourrous et al., 2018). This comparison is shown in the SI.1.3. It is also likely that the effects of C_{ov} and primary particle overlapping are implicitly captured by the simplified FA model (Eq. 15) via inputs of k_a and D_α (or D_{fm}), given the observations of Oh & Sorensen (1997) where it is shown that these parameters tend to increase with C_{ov}.

For these reasons, the simplified version of the FA model (Eq. 15) is selected for ease of application. Nevertheless, we have outlined the full derivation of the FA model in Eq. 16 for potential use in future applications when more data on the changes in C_{ov} for different BC emissions source and engine settings become available. In Section 5, we revisit the sensitivity of the FA model to C_{ov} in relation to uncertainties introduced by other parameters.

In summary, the FA model is capable of estimating: (i) the BC PN emissions from various emission sources when inputs of mass (M or EI_m), PSD (GMD and GSD), and morphology (k_a, D_α, k_{TEM} and D_{TEM}) are available; (ii) the BC M (or emissions factor) for various sources with inputs of N (or emissions factor), PSD and morphology; (iii) the GMD and GSD of the BC aggregates if morphology, number and mass measurements are present; or (iv) the morphology (k_a and D_α) if the PSD, number and mass data are available. For this paper, we will focus on application (i) where the FA model is used to estimate BC PN emissions from mass and PSD. Figure 1 shows a flow chart outlining the input parameters and procedure required to apply the FA model for this particular application.

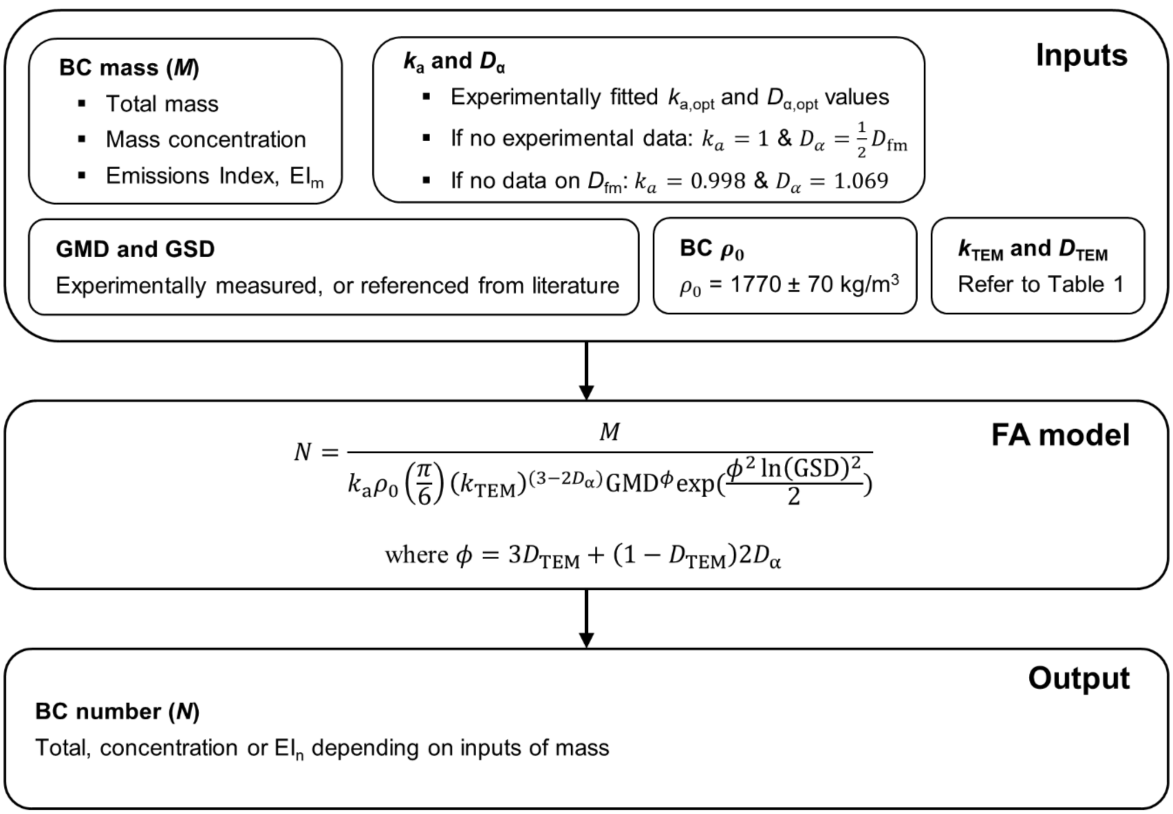

Figure 1: Flow chart outlining the parameters and procedure required to implement the FA model in estimating BC PN emissions from inputs of mass, PSD and morphology.

3 Materials and methods

The datasets and estimated input variables used to validate the FA model are summarised in Table 3. For further methodological details, the reader is referred to SI.3. Specific datasets are described in Sections 3.1 (CIDI engine), 3.2 (soot generator) and 3.3 (aircraft gas turbine engines at ground and cruise conditions).

All measurements included in this study are derived from experiments that included a volatile particle remover (thermodenuder or catalytic stripper). We therefore assume that the aggregates and primary particles consist purely of BC with a constant ρ_0 value of 1770 kg m^{-3} (Park et al., 2004). The uncertainty in ρ_0 is discussed in Section 5. For the aircraft gas turbine dataset, Crayford et al. (2012) found negligible mass concentrations of organic carbon downstream of the catalytic stripper. Furthermore, other studies have shown high volatile particle removal efficiencies in other applications; for example, Giechaskiel et al. (2010) showed that the mass-based removal efficiency of volatile and semi-volatile particles is > 99% for nucleation mode particles and an efficiency of 50 to 90% for particles in the accumulation mode.

We also note that correction factors on particle losses along the sampling lines were not applied in all four datasets due to large uncertainties. Hence, all the data used to validate the FA model represents measurements at the instrument sampling point instead of the point of emission.

3.1 CIDI engine data

BC emissions and aggregate morphology data from a six-cylinder CIDI engine were obtained from Graves et al. (2015), the dataset from which consists of 16 data points corresponding to six different engine operating conditions. Exhaust gas was sampled and diluted at a ratio of 11:1 before passing through a thermodenuder to remove volatile materials. A scanning mobility particle sizer (SMPS) measured the PSD of the non-volatile PM (assumed to be primarily BC), from which data was subsequently used to calculate the PSD (GMD and GSD) and the measured BC PN concentration (N). Due to the lack of a separate CPC, data from the SMPS is used as a reference for the measured N. The total BC mass concentration (M) was estimated using the integrated particle size distribution (IPSD) method (Liu et al., 2009).

Particle line loss correction factors were only applied to account for diffusional losses in the thermodenuder, while DMA measurements were not corrected for diffusion and multiple charging effect (Graves, 2019). Given that the DMA and thermodenuder are located upstream of the CPC and CPMA, we note that the effects for the corrections applied (or lack of) are consistent in the measured PSD, and therefore the calculated M and N.

Table 3: Summary of the four datasets used to validate the FA model. The sources of certain input variables that are required by the FA model are also listed. Specific references are denoted by square brackets.

§	Emissions Source	Data Points	Measured Quantity	Empirically fitted & Estimated Parameters	Volatile Particle Remover	Particle Line Loss Corrections	Ref.
3.1	CIDI Engine: Six-cylinder Cummins ISX	16 data points measured from 6 engine operating conditions.	N (SMPS) GMD GSD ρ_{eff}	Fitted [2]: $k_{a,opt}$ $D_{\alpha,opt}$ Estimated: M [6] ρ_0 [8] k_{TEM} [4] D_{TEM} [4]	TN	Corrected for diffusional deposition losses along thermodenuder. No corrections applied to DMA measurements and particle losses along the sampling line.	[2], [4], [6], [8]
3.2	Soot Generator	13 data points measured from laboratory experiments	N (CPC) GMD GSD M	Estimated: ρ_0 [8] k_{TEM} [4] D_{TEM} [4] k_a=0.998 [5] D_α=1.069 [5]	CS	No corrections applied to account for particle losses in the sampling line. Diffusion and multiple charge correction applied to PSD measured by SMPS.	[4], [8]
3.3	Aircraft Gas Turbine @ ground level: CFM56-5B4-2P	SAMPLE III.2 - Ground Measurements 37 data points measured from 24 different F/F_{00}	EI_n (DMS) GMD GSD EI_m	Assumptions [5]: $k_a = 1$ $D_{fm} = 2D_\alpha$ Estimated: ρ_0 [8] k_{TEM} [4] D_{TEM} [4] D_{fm} [9]	CS	No corrections applied due to large uncertainties in the line loss correction factors. Internal particle charge correction and aggregate model applied to DMS measurements.	[1], [4], [5], [8]
	Aircraft Gas Turbine @ cruise altitudes: CFM-56-2-C1	NASA ACCESS – Cruise Measurements 12 data points measured from 3 different F/F_{00}	EI_n (CPC) GMD GSD EI_m	Assumptions [5]: $k_a = 1$ $D_{fm} = 2D_\alpha$ Estimated: ρ_0 [8] k_{TEM} [4] D_{TEM} [4] D_{fm} [9]	TN	Particle losses in the probe inlet and sampling lines have been estimated but not applied due to large uncertainties.	[4], [5], [7], [8]

[1] Boies et al. (2015) [4] Dastanpour & Rogak (2014) [7] Moore et al. (2017)
[2] Dastanpour et al. (2016) [5] Eggersdorfer et al. (2012b) [8] Park et al. (2004)
[3] Dastanpour et al. (2017) [6] Graves et al. (2015) [9] Table 4, main text

Volatile Particle Remover: TN = Thermodenuder; CS = Catalytic stripper

Using the same CIDI engine, Dastanpour et al. (2016) optimised the k_a and D_α values for each engine operating mode, which will be referred to as $k_{a,opt}$ and $D_{\alpha,opt}$. The performance of the FA model will be compared by using (i) $k_{a,opt}$ and $D_{\alpha,opt}$ values from Dastanpour et al. (2016) (listed in the SI.3.1), and (ii) the constant k_a = 0.998 and D_α = 1.069 values (Eggersdorfer et al., 2012b) in Section 4.1. k_{TEM} and D_{TEM} coefficients of 2.644×10^{-6} and 0.39 (Table 1) are used for all engine modes in the FA model.

3.2 Soot generator data

A laboratory-based experiment was conducted to measure the concentration and characteristics of BC aggregates produced by a soot generator, where BC aggregates are produced by mixing propane (C_3H_8), nitrogen (N_2), and air in a co-flow inverse diffusion flame (Stettler et al., 2013b).

In total, this experiment generated 13 data points that are used to validate the FA model. The BC concentration and size distribution are controlled by changing the residence time and dilution ratio in the ageing chamber and ejector diluter. A catalytic stripper is then connected downstream to remove volatile particles before parallel measurements of N (CPC, used as reference for measured N), M (Micro-Aethalometer AE51), and the PSD (SMPS) are taken. Diffusion and multiple charge correction have been applied for PSD measurements taken by the SMPS. Further details on this experiment can be found in SI.3.2.

The assumed k_{TEM} and D_{TEM} coefficients are 2.465×10^{-6} and 0.29 respectively (Table 1), while constant values of k_a = 0.998 and D_α = 1.069 (Eggersdorfer et al., 2012b) were used due to the lack of data on the $k_{a,opt}$ and $D_{\alpha,opt}$ values. Like the CIDI engine, the validation results will be presented in the form of parity plots in Section 4.2.

3.3 Aircraft gas turbine engine data

Aircraft BC emissions and aggregate morphology data are compiled from two experimental campaigns at ground and cruise conditions.

Ground-level BC measurements for a CFM56-5B4-2P double annular combustor (DAC) engine, consisting of 37 data points measured from 24 different engine thrust settings are taken from the SAMPLE III.2 campaign (Boies et al., 2015). All instruments were located downstream of a catalytic stripper to eliminate the presence of volatile materials. Measurements include PSD and

EI_n by DMS500 nanoparticle size spectrometer (Cambustion), and EI_m by laser induced incandescence (LII). An internal particle charge correction and an aggregate model has been accounted in the measurements made by the DMS. Although the EI_n is also measured by a separate CPC (TSI Model 3772, 10 nm D_{50}), we used the DMS measured EI_n as a reference because it has a lower cut-off point of 5 nm relative to 10 nm for the CPC. Line loss correction factors for similar experiments can exceed a factor of 5 for particles with d_m < 10 nm (Durdina et al., 2014). However, given significant uncertainties in these correction factors, neither the PSD, EI_n or EI_m were corrected for sampling losses and so the validation presented in this study is representative of the instrument measurement point, rather than the engine exit plane.

Cruise-level BC measurements from a DC-8 aircraft equipped with a CFM56-2-C1 single annular combustor (SAC) engine are from the NASA ACCESS campaign (Moore et al., 2017). This dataset includes measurements of EI_n by a CPC (used as reference for the measured EI_n), GMD and GSD by an SMPS located downstream of a thermodenuder, while EI_m is measured with a particle soot absorption photometer (PSAP). Particle losses in the probe inlet and sampling lines have been estimated (accounting for diffusional, inertial and sedimentation losses) but these correction factors were not applied to the measured BC EI_n, EI_m and the PSD due to large uncertainties (Moore et al., 2017).

Two different k_{TEM} and D_{TEM} values for aircraft gas turbine engines from Dastanpour & Rogak (2014) and Boies et al. (2015) are listed in Table 1. The sensitivity of the FA model to these values is evaluated for ground and cruise-level measurements.

For both ground and cruise conditions, we assume that $k_\alpha = 1$ and $D_\alpha = \frac{1}{2} D_{fm}$ (Eggersdorfer et al., 2012b) due to a lack of data on the variation of k_a and D_α values across aircraft engine thrust settings (F/F_{00}). These assumptions are supported by Boies et al. (2015) and Liati et al. (2014). Further information can be found in SI.2. By specifying the assumptions of $k_\alpha = 1$ and $D_\alpha = \frac{1}{2} D_{fm}$ for aircraft BC emissions, Eq. 8 becomes,

$$n_{pp} = \left(\frac{d_m}{d_{pp}}\right)^{D_{fm}}, \quad (17)$$

which was also specified in existing literature (Rogak et al., 1993; Sorensen, 2011). D_{fm} measurements are not provided by Boies et al. (2015) and Moore et al. (2017), however they can be estimated based on other literature. Table 4 lists the D_{fm} values for both SAC and DAC aircraft gas turbine engines at different operating conditions. D_{fm} values for SAC engines are interpolated from Durdina et al. (2014) and Abegglen et al. (2015). The increasing D_{fm} values with F/F_{00} indicate that BC aggregates are increasingly spherical at higher F/F_{00}. Since the range of D_{fm} for a DAC engine is relatively limited (2.73 to 3) across different F/F_{00}, a nominal D_{fm} value of 2.76 is used (Johnson et al., 2015). For cruise conditions, we assume a fixed D_{fm} value of 2.76 for both SAC and DAC engines. This is justified as the turbine and compressor inlet temperature ratio (T_4/T_2), which approximates the non-dimensional engine thrust setting, at cruise and take-off conditions are within 5% (Cumpsty, 2003).

The performance of the FA model is also compared with previous methodologies from Döpelheuer (2002) and Barrett et al. (2010b) by validating it with the same ground- and cruise-level datasets.

Table 4: Specification of D_{fm} input values for different aircraft engine operating conditions.

Combustor Type	Operating Condition	Specification of D_{fm} Inputs - Turbofan Engine		Reference
SAC	Ground	D_{fm} = 2.37	, $0.03 \leq \frac{F}{F_{00}} < 0.15$	[1]
		D_{fm} = 2.50	, $0.15 \leq \frac{F}{F_{00}} < 0.30$	
		D_{fm} = 2.57	, $0.30 \leq \frac{F}{F_{00}} < 0.50$	
		D_{fm} = 2.64	, $0.50 \leq \frac{F}{F_{00}} < 0.70$	
		D_{fm} = 2.76	, $0.70 \leq \frac{F}{F_{00}} < 1.00$	[2]
DAC	Ground	D_{fm} = 2.76	, $0.03 \leq \frac{F}{F_{00}} < 1.00$	[3]
SAC & DAC	Cruise	D_{fm} = 2.76	, $0.03 \leq \frac{F}{F_{00}} < 1.00$	Justification in text

[1] Durdina et al. (2014) [2] Abegglen et al. (2015) [3] Johnson et al. (2015)

4 Validation of the FA Model

This section presents the validation of the FA model with different soot emission sources: an internal combustion engine in Section 4.1, a soot generator in Section 4.2, and two aircraft gas turbine engines operating at ground and cruise conditions in Section 4.3.

4.1 CIDI engine

The parity plot in Figure 2a shows the validation results with emissions data from the CIDI internal combustion engine, where $k_{a,opt}$ and $D_{\alpha,opt}$ values for each engine modes are used. The estimated N from the measured mass is in good agreement with the measured N for the CIDI engine ($R^2 = 0.939$) and the average NMB values show that N is underestimated by 8.3%. All the data points agree to within ±30% of the measured N.

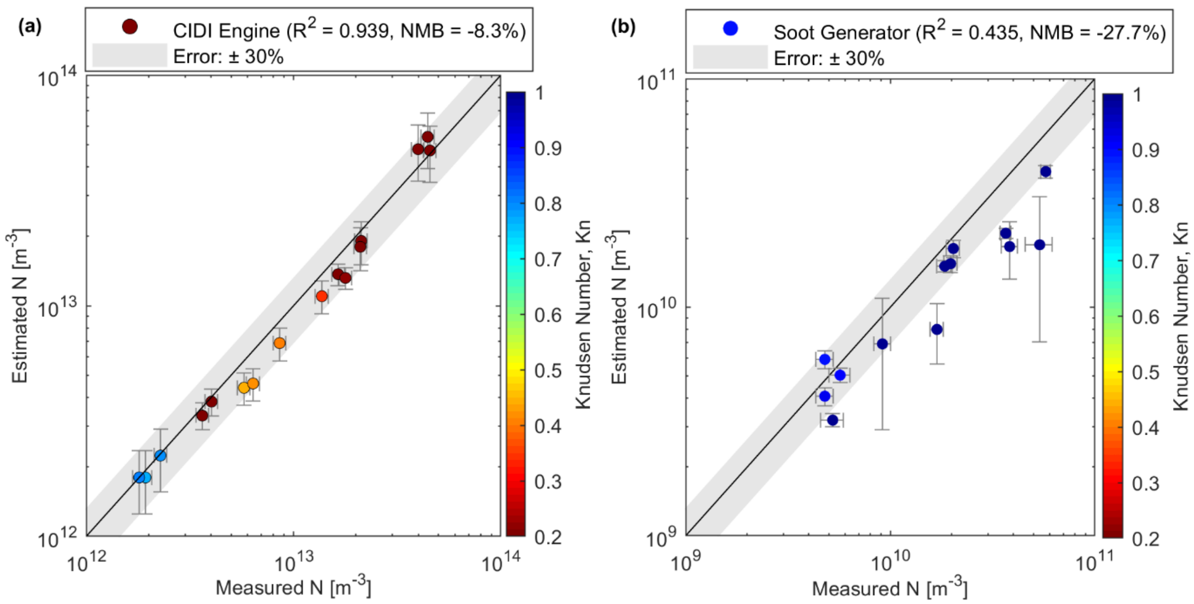

Figure 2: Validation of the FA model against emissions from a (a) CIDI engine where $k_{a,opt}$ and $D_{\alpha,opt}$ values are used, and (b) a soot generator where constant values of $k_a = 0.998$ and $D_\alpha = 1.069$. Error bars denote precision errors from repeated measurements at a 95% confidence interval. Detailed data tables can be found in SI.4 and SI.5.

Additionally, the CIDI engine is also validated by using constant values of $k_a = 0.998$ and $D_\alpha = 1.069$ (Eggersdorfer et al., 2012b) and the results are shown in SI.4. The R^2 value remains high at 0.978 but the NMB exhibited a small increase where N is overestimated by 15.5% on average. 14 of the 16 data points (88%) agree to within ±30% of the measured N. Therefore, we conclude that the two sets of k_a and D_α values do not lead to significant discrepancies in the FA model output when used to estimate BC emissions from a CIDI engine, and can be used when more accurate $k_{a,opt}$ and $D_{\alpha,opt}$ data are unavailable for a given engine type, operating condition or emission source.

4.2 Soot generator

Figure 2b shows the FA model validation against emissions from a soot generator, where constant values of $k_a = 0.998$ and $D_\alpha = 1.069$ (Eggersdorfer et al., 2012b) were used. Although 9 of the 13 data points (69%) agree to within ±30% of the measured N, the R^2 and NMB are 0.435 and -27.7% respectively. One potential source of this systematic negative bias in estimated N is a bias in the Micro-Aethalometer measurements of M; negative biases of up to 70% can result from cumulative loading of BC on the filter substrate (Good et al., 2017). Furthermore, 3 of the 4 outliers have the lowest measurements of M (0.380 to 0.768 μg m^{-3}), and therefore are most affected by measurement uncertainties (± 0.1 μg m^{-3}) of 13% to 26% (AethLabs, 2016). These two uncertainties, as well as the use of constant k_a and D_α values could be the contributors to the reduction in performance for the FA model relative to the CIDI engine.

4.3 Aircraft gas turbine engines

Two distinct validation tests are conducted to select a suitable coefficient pair (k_{TEM} and D_{TEM}) for the FA model to estimate aircraft BC emissions. Figure 3 shows the parity plots for the FA model validation using k_{TEM} and D_{TEM} coefficients of 1.621×10^{-5} and 0.39 respectively (Dastanpour & Rogak, 2014).

For ground conditions (Figure 3a), estimated EI_n are in good agreement with measured EI_n (R^2 = 0.950), while the NMB shows that the average EI_n is overestimated by 27%. 77% of data points agree to within ±30% of the measured EI_n, and 83% agree when error bars are included. The overestimation of EI_n is significant at thrust settings above 50% F/F_{00}, where the NMB increases to around 163% (data points with lower EI_n values). This could be due to the assumption of DLCA ($Kn \geq 1$) in the derivation of the FA model; at high thrust conditions, observations from TEM images suggest that BC primary particles are often highly sintered (Liati et al., 2014) and at high primary particle concentrations, BC aggregates are formed in the continuum and transition regime ($Kn < 1$). The decrease in the Kn as F/F_{00} increase (shown in the colour bar of Figure 3a) creates an environment for BC aggregates to form in a reaction-limited cluster aggregation (RLCA) (Bisson et al., 2016; Vander Wal et al., 2014). Therefore, the assumption of a free molecular flow regime ($Kn \geq 1$) adopted in Eq. 8 and Eq. 17 could be violated at higher F/F_{00}. Eggersdorfer et al. (2012a) suggested that the measured and estimated d_m differs by around 10% to 20% when Eq. 8 and Eq. 17 are applied in the transition regime (up to $Kn = 0.28$). Although this additional uncertainty could be the source of the increase in NMB values for the FA model at low Kn, it was not observed in the validation of the CIDI engine (Section 4.1), possibly due to the use of more accurate $k_{a,opt}$ and $D_{\alpha,opt}$ values for each engine modes, and these results indicate that the effects of C_{ov} could be implicitly accounted for in the $k_{a,opt}$ and $D_{\alpha,opt}$ constants.

Figure 3b presents results for the FA model validation against cruise measurements. Due to the lower ambient pressure and F/F_{00} required in cruise conditions, the BC aggregates are all formed in the free-molecular regime (Kn ≥ 1). The overall R^2 value (R^2 = 0.684) is slightly lower than with the ground-level validation. However, the overall NMB is +2.4%. 75% of data points agree to within ±30% of the measured EI_n, and 100% agree when error bars are included. Cruise measurements are more challenging to perform relative to ground experiments; different factors such as the variability in plume sampling distance (Moore et al., 2017), particle bouncing (Korolev et al., 2013) and instrument detection limits (Baumgardner et al., 2017; Schumann et al., 2013) contribute to an increased uncertainty in the PSD and EI_n measurements at cruise. Notably, the outlier with the largest error bar in the estimated EI_n is caused by large uncertainties in the measured GMD and GSD (±13% each), relative to an average uncertainty of ±2% for all other data points.

Measurements at cruise include tests using a 50:50 HEFA low-sulphur content Jet A fuel blend, which make up half of the EI_n data points are also shown in figure 3b. The validation results do not show a large discrepancy between conventional (R^2 = 0.783) and alternative fuel scenarios (R^2 = 0.564). Hence, we conclude that the FA model can also be applied to different fuel types, if changes in the EI_m, GMD and GSD are known.

The FA model exhibited minor performance improvements using the k_{TEM} and D_{TEM} coefficients by Dastanpour & Rogak (2014) compared to when the coefficients from Boies et al. (2015) are used; average R^2 values decreased from 0.817 to 0.805, while the NMB increased from 15% to 23% relative to using coefficients from Dastanpour & Rogak (2014) (SI.6.2). Therefore, we recommend that the k_{TEM} and D_{TEM} coefficient pair from Dastanpour & Rogak (2014) is used in future studies to estimate the EI_n for aircraft emissions.

When k_a and D_α values of 0.998 and 1.069 (Eggersdorfer et al., 2012b) are applied to aircraft datasets, however, we obtain a significantly lower R^2 and higher NMB values when validated against ground ($R^2 = -0.03, \mathrm{NMB} = +123\%$) and cruise-level ($R^2 = -3.03, \mathrm{NMB} = +76\%$)

measurements (shown in SI.6.3). This could be due to the differences in aircraft BC aggregate morphology relative to other emission sources. Ghazi et al. (2013) identified that the assumption of $D_\alpha = 1.069$ is only valid when d_{pp} and d_m have a low correlation. However, Table 1 shows that the D_{TEM} values for aircraft gas turbine engines are the highest among all emission sources. The higher sensitivity of d_{pp} to the changes in d_m suggests that the value of D_α for aircraft BC aggregates could be higher than 1.069.

Finally, both ground and cruise validation for previous BC EI_n methodologies (Barrett et al., 2010b; Döpelheuer, 2002) are presented in SI.7.2. For ground and cruise validations, R^2 values from previous methodologies range between -0.34 and 0.70, while the NMB vary from -78% to -4%. These results show that the FA model significantly improves the EI_n prediction accuracy for aircraft emissions relative to previous methods in terms of R^2 and NMB values.

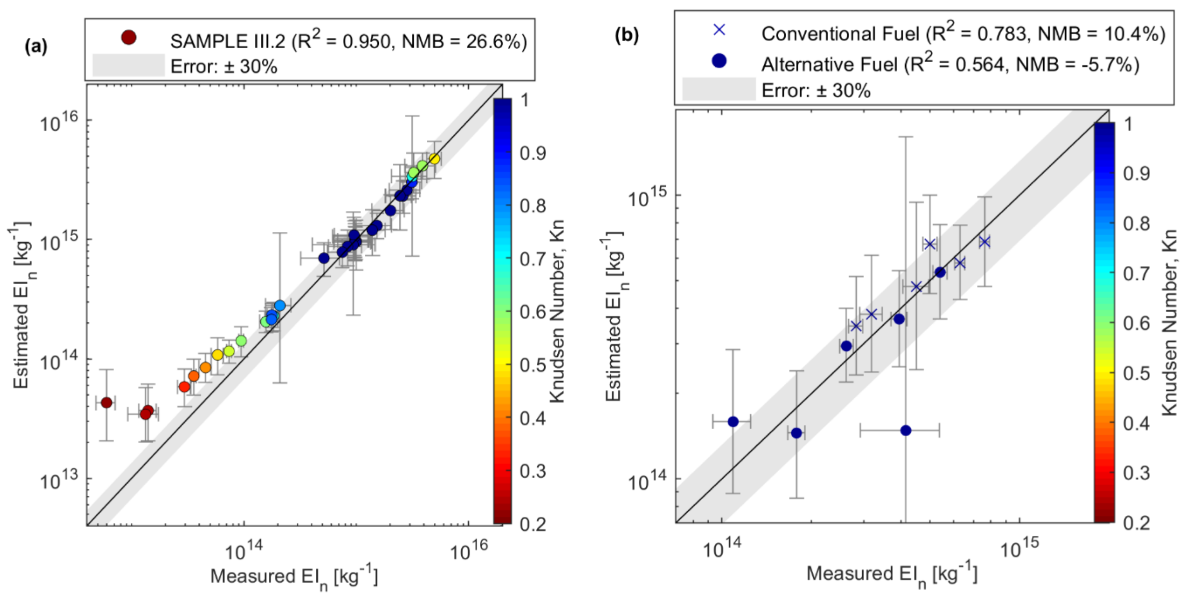

Figure 3: Validation of the FA Model for aircraft (a) ground conditions using data from Boies et al. (2015), and (b) cruise conditions using data from Moore et al. (2017). k_{TEM} and D_{TEM} prefactor-exponent coefficients specified by Dastanpour & Rogak (2014), $k_{TEM} = 1.621\text{x}10^{-5}$ and $D_{TEM} = 0.39$ are used. Error bars denote precision errors from repeated measurements at a 95% confidence interval and do not include systematic uncertainties arising from instrumentations. Detailed data tables, equations, as well as ground validation for previous EI_n methodologies not presented in this figure can be found in SI.6 and SI.7.

5 Uncertainty and Sensitivity Analysis

In Section 5.1, we first quantify the uncertainties for different input parameters of the FA model and how they propagate forward to uncertainty in the estimated N or EI_n. Section 5.2 then evaluates the sensitivity of the FA model output to the input parameters, highlighting the most important parameters and priorities for future research.

5.1 Uncertainty Analysis

Uncertainties are classified into two types: (i) Type A (or precision) uncertainty that is statistically estimated from repeated measurements, and (ii) Type B (or systematic/bias) uncertainty that is analytically estimated from other data sources (Coleman & Steele, 2009). To the best of our ability, we compiled the precision and/or systematic errors for the measured N (or EI_n) and each input parameter of the FA model (M, GMD, GSD, ρ_0, k_a, D_α, D_{fm}, k_{TEM} and D_{TEM}) depending on the data availability. The uncertainty of each model input parameter is then propagated forward to estimate the uncertainties of the FA model output (estimated N or EI_n) and to conduct a sensitivity analysis.

Table 5 presents the estimated uncertainties for each variable in the FA model. For the uncertainty values that are experimentally estimated: N_{CPC} (± 2.8%), M_{LII} (± 25%), D_{fm} (± 7.9%) and ρ_0 (± 7.8%), we assume that both the systematic and precision uncertainty have been captured in the standard deviation of repeated measurements. The systematic error for M_{IPSD} (±11.4%) is analytically estimated by propagating the measurement errors from instruments (DMA-CPMA-CPC) with the Root-Sum-Square method. Although a similar propagation of error method estimates the uncertainties of GMD and GSD to be ± 4.97% and ± 6.13% respectively, we have increased their respective uncertainties to the maximum tolerable uncertainty of ± 10%, which is in accordance to the calibration standards specified by the European Center for Aerosol Calibration (ECAC) and the World Calibration Center for Aerosol Physics (WCCAP). This is because we are unable to quantify the additional uncertainties resulting from the inversion method, bipolar diffusion charging and the DMA transfer function (Wiedensohler et al., 2018). Systematic errors for k_{TEM} (± 29.4%) and D_{TEM} (± 17.8%) are estimated using the 95% confidence intervals that were published in Table S1 of Dastanpour & Rogak (2014), while numerical simulation results from Eggersdorfer & Pratsinis (2012) are used to estimate the precision uncertainties for k_a (± 1.2%) and D_α (± 0.3%). Detailed calculations regarding the uncertainty quantification for each variable are presented in SI.9.

Given the non-linear nature of the FA model and the potential presence of covariance between uncertainty variables ($\sigma_{AB} \neq 0$), the numerical Monte Carlo Method is selected instead of the analytical Taylor Series Method to quantify the total uncertainty of the FA model output, the estimated N or EI_n (Coleman & Steele, 2009). We note that 10,000 Monte Carlo runs were performed for the standard deviation of the error distribution to converge to below 1% (Coleman & Steele, 2009). Since the distribution of experimental errors is typically assumed to be normal (Peters, 2001), a normal distribution is specified for the model input parameters specified in Table 5. Conversely, we assume that C_{ov} is uniformly distributed within the range of 0.02 and 0.24 as reported in Bourrous et al. (2018) due to the lack of knowledge regarding its uncertainty distribution.

Table 5: Systematic and/or precision uncertainties for each variable in the FA model.

Variables in the FA Model	Uncertainty Estimation Methodology (Measuring Instruments)	Systematic Uncertainty (95% C.I.)	Precision Uncertainty (95% C.I.)	References
Measured N / EI_n	Experimental (CPC)	$\Sigma \approx \pm$ 2.8%		[8]
M / EI_m	Experimental (LII)	$\Sigma \approx \pm$ 25%		[2], [6]
	Analytical (IPSD: DMA–CPMA–CPC)	± 11.4%	-	[5], [7], [8]
GMD	ECAC & WCCAP calibration standards	± 10%	-	[10]
GSD	ECAC & WCCAP calibration standards	± 10%	-	[10]
k_{TEM}	Experimental (TEM) – Aircraft	± 32.9%	-	[3]
	Experimental (TEM) – CIDI/HPDI	± 15.9%	-	[3]
D_{TEM}	Experimental (TEM) – Aircraft	± 18.0%	-	[3]
	Experimental (TEM) – CIDI/HPDI	± 10.3%	-	[3]
k_a	Numerical simulation	-	± 1.20%	[4]
D_α	Numerical simulation	-	± 0.30%	[4]
D_{fm}	Experimental	$\Sigma \approx \pm$ 7.88%		[1]
ρ_0	Experimental	$\Sigma \approx \pm$ 7.75%		[9]

[1] Abegglen et al. (2016)
[2] Boies et al. (2015)
[3] Dastanpour & Rogak (2014)
[4] Eggersdorfer & Pratsinis (2012)
[5] Kinney et al. (1991)
[6] Lobo et al. (2015a)
[7] Olfert et al. (2017)
[8] Owen et al. (2012)
[9] Park et al. (2004)
[10] Wiedensohler et al. (2018)

Firstly, for aircraft emissions using data from the SAMPLE III.2 campaign (Boies et al., 2015), the errors of the FA model outputs are asymmetrically distributed with an uncertainty bound of $(-54\%, +103\%)$ at a 95% confidence interval. Secondly, using measured data from the CIDI engine (Graves et al., 2015), the 95% confidence interval is $(-44\%, +79\%)$. This is smaller than the uncertainty bound for the aircraft gas turbine engine because of the lower uncertainty values in the input parameters: M_{IPSD} (± 11.4%), k_{TEM} (± 15.9%) and D_{TEM} (± 10.3%). Detailed calculations and results are presented in SI.9.2. We note that the uncertainty bounds are asymmetric because of the non-linearity of the FA model and the large uncertainties for most input variables (>5%) (Coleman & Steele, 2009). Overall, the quantified uncertainty bounds of the FA model outputs present an advance in understanding relative to previous methodologies used to estimate aircraft BC PN emissions (Barrett et al., 2010b; Döpelheuer, 2002), where an uncertainty analysis was not conducted.

5.2 Sensitivity Analysis

A variance-based global sensitivity analysis is conducted using the Sobol' method (Saltelli et al., 2008) to rank and identify input parameters that contribute to the highest variance in the FA model output. Detailed results of the sensitivity analysis are presented in SI.9.3.

The results indicate that the GSD contributes to the largest sensitivity in the FA model output (estimated N or $\mathrm{EI_n}$), followed by D_{TEM}, GMD and the measured M_{LII}. A ± 10% change in GSD will result in variations in estimated N or $\mathrm{EI_n}$ of - 37% to + 53%. Therefore, these results suggest that measurements of M, D_{TEM}, GMD and GSD should be prioritised to reduce the uncertainty bounds of the FA model output. New and standardised measurement procedures recommended by the PMP and ICAO's forthcoming aircraft nvPM standard (ICAO, 2016) could also facilitate reductions in the uncertainties of these individual parameters and subsequently the uncertainty bounds of the FA model output. Conversely, we note that input parameters of k_{a}, C_{ov} and BC ρ_0 contribute to the lowest sensitivity to the estimated N or $\mathrm{EI_n}$. This suggests that the assumptions of (i) $k_a = 1$ for aircraft emissions across all engine type and thrust settings, (ii) a single point of contact between pairs of primary particles ($C_{\mathrm{ov}} = 0$), and (iii) a constant material density of BC aggregates would not significantly affect the outputs of the simplified FA model (Eq. 15).

6 Conclusions

BC PN emissions lead to adverse health and environmental effects and must be measured/modelled more accurately to reduce its associated uncertainties. This paper critically reviews the theory of fractal aggregates and develops a methodology capable of estimating BC PN emissions from mass. The new methodology, named as the FA model (Eq. 15), overcomes the limitations inherent in previous methodologies used to estimate BC PN emissions where simplifying assumptions were made (e.g. constant PSD and morphology).

We have validated the FA model with three different BC emission sources: a CIDI engine ($\mathrm{R}^2 = 0.94$, $\mathrm{NMB} = -8.3\%$), a soot generator ($\mathrm{R}^2 = 0.44$, $\mathrm{NMB} = -27.7\%$), as well as aircraft gas turbine engines at ground ($\mathrm{R}^2 = 0.95$, $\mathrm{NMB} = +26.6\%$) and cruise conditions ($\mathrm{R}^2 = 0.68$, $\mathrm{NMB} = +2.4\%$). For aircraft PN emissions, these results show a significant improvement relative to previous aircraft $\mathrm{EI_n}$ estimation methodologies (Average $\mathrm{R}^2 = 0.10$, $\mathrm{NMB} = -36\%$) when validated with the same aircraft datasets at ground and cruise.

Uncertainty analysis conducted using the numerical Monte Carlo method estimates N or $\mathrm{EI_n}$ to have an asymmetrical uncertainty bound of $(-54\%, +103\%)$ at a 95% confidence interval for aircraft gas turbine engines, and $(-44\%, +79\%)$ for a CIDI engine. A variance-based global sensitivity analysis identified that uncertainties in the GSD contribute to the largest sensitivity in the FA model outputs, while having a low sensitivity to input parameters of k_a, $\mathrm{C_{ov}}$ and ρ_0.

We have demonstrated potential applications of the FA model, in particular to estimate BC PN emissions from various combustion sources using inputs of mass, PSD and morphology. Given that BC mass measurements and models are more commonly available than PN, BC PN can now be estimated for a range of studies, including health impact and aviation contrail analyses. Further applications of the FA model include estimating BC: (i) mass from number, PSD and morphology; (ii) PSD from mass, number and morphology inputs; and (iii) morphology from mass, number and PSD estimates.

Acknowledgements

Roger Teoh received funding from The Lloyds Register Foundation, and the Skempton Scholarship from the Department of Civil and Environmental Engineering, Imperial College London. Qing Wang (Imperial College London), Robert Nishida and Mario Schriefl (University of Cambridge) collected the data from the soot generator experiments. Ramin Dastanpour and

Steven Rogak (University of British Columbia) provided data used in the early development of the FA model.

References

Abdul-Khalek, I. S., Kittelson, D. B., Graskow, B. R., Wei, Q., & Bear, F. (1998). Diesel exhaust particle size: measurement issues and trends.

Abegglen, M., Brem, B. T., Ellenrieder, M., Durdina, L., Rindlisbacher, T., Wang, J., … Sierau, B. (2016). Chemical characterization of freshly emitted particulate matter from aircraft exhaust using single particle mass spectrometry. *Atmospheric Environment*, *134*, 181–197.

Abegglen, M., Durdina, L., Brem, B. T., Wang, J., Rindlisbacher, T., Corbin, J. C., … Sierau, B. (2015). Effective density and mass-mobility exponents of particulate matter in aircraft turbine exhaust: Dependence on engine thrust and particle size. *Journal of Aerosol Science*, *88*, 135–147. https://doi.org/10.1016/j.jaerosci.2015.06.003

AethLabs. (2016). MicroAeth AE51 Operating Manual. Retrieved from https://aethlabs.com/microaeth/ae51/overview

Anderson, B. E., Beyersdorf, A. J., Hudgins, C. H., Plant, J. V, Thornhill, K. L., Winstead, E. L., … Miake-Lye, R. C. (2011). Alternative aviation fuel experiment (AAFEX).

Barrett, S. R. H., Britter, R. E., & Waitz, I. A. (2010a). Global mortality attributable to aircraft cruise emissions. *Environmental Science & Technology*, *44*(19), 7736–7742.

Barrett, S. R. H., Prather, M., Penner, J., Selkirk, H., Balasubramanian, S., Döpelheuer, A., … Hileman, J. (2010b). Guidance on the use of AEDT gridded aircraft emissions in atmospheric models. *US Federal Aviation Administration Office of Environment and Energy*.

Baumgardner, D., Abel, S. J., Axisa, D., Cotton, R., Crosier, J., Field, P., … Kraemer, M. (2017). Cloud ice properties: in situ measurement challenges. *Meteorological Monographs*, *58*, 9.1-9.23.

Bisson, J., Seers, P., Huegel, M., & Garnier, F. (2016). Numerical prediction of gaseous aerosol precursors and particles in an aircraft engine. *Journal of Propulsion and Power*, *32*(1), 918–928.

Boies, A. M., Stettler, M. E. J., Swanson, J. J., Johnson, T. J., Olfert, J. S., Johnson, M., … Thomson, K. (2015). Particle emission characteristics of a gas turbine with a double annular combustor. *Aerosol Science and Technology*, *49*(9), 842–855.

Bond, T. C., Doherty, S. J., Fahey, D. W., Forster, P. M., Berntsen, T., DeAngelo, B. J., … Koch, D. (2013). Bounding the role of black carbon in the climate system: A scientific assessment. *Journal of Geophysical Research: Atmospheres*, *118*(11), 5380–5552.

Boucher, O. (2011). Atmospheric science: Seeing through contrails. *Nature Climate Change*, *1*(1), 24–25.

Bourrous, S., Ribeyre, Q., Lintis, L., Yon, J., Bau, S., Thomas, D., … Ouf, F.-X. (2018). A semi-automatic analysis tool for the determination of primary particle size, overlap coefficient and specific surface area of nanoparticles aggregates. *Journal of Aerosol Science*, *126*, 122–132.

Brasil, A. M., Farias, T. L., & Carvalho, M. G. (1999). A recipe for image characterization of fractal-like aggregates. *Journal of Aerosol Science*, *30*(10), 1379–1389.

Brasseur, G. P., Gupta, M., Anderson, B. E., Balasubramanian, S., Barrett, S., Duda, D., … Gettelman, A. (2016). Impact of Aviation on Climate: FAA's Aviation Climate Change Research Initiative (ACCRI) Phase II. *Bulletin of the American Meteorological Society*, *97*(4), 561–583.

Burkhardt, U., Bock, L., & Bier, A. (2018). Mitigating the contrail cirrus climate impact by reducing aircraft soot number emissions. *Npj Climate and Atmospheric Science*, *1*(Article number: 37). Retrieved from https://www.nature.com/articles/s41612-018-0046-4

Burtscher, H. (2005). Physical characterization of particulate emissions from diesel engines: a review. *Journal of Aerosol Science*, *36*(7), 896–932.

Caiazzo, F., Agarwal, A., Speth, R. L., & Barrett, S. R. H. (2017). Impact of biofuels on contrail warming. *Environmental Research Letters*, *12*(11), 114013.

Coleman, H. W., & Steele, W. G. (2009). *Experimentation, validation, and uncertainty analysis for engineers*. John Wiley & Sons.

Crayford, A., Johnson, M., Marsh, R., Sevcenco, Y., Walters, D., Williams, P., … Lister, D. (2012). *SAMPLE III: Contribution to aircraft engine PM certification requirement and standard Second Specific Contract - Final Report*. Retrieved from https://www.easa.europa.eu/sites/default/files/dfu/SAMPLE III-SC02 Final report.pdf

Cumpsty, N. (2003). Jet Propulsion. A simple guide to the aerodynamic and thermodynamic design and performance of jet engines. Second Edition, *1*, 13.

Dastanpour, R., Momenimovahed, A., Thomson, K., Olfert, J., & Rogak, S. (2017). Variation of the optical properties of soot as a function of particle mass. *Carbon*, *124*, 201–211.

Dastanpour, R., & Rogak, S. N. (2014). Observations of a correlation between primary particle and aggregate size for soot particles. *Aerosol Science and Technology*, *48*(10), 1043–1049.

Dastanpour, R., Rogak, S. N., Graves, B., Olfert, J., Eggersdorfer, M. L., & Boies, A. M. (2016). Improved sizing of soot primary particles using mass-mobility measurements. *Aerosol Science and Technology*, *50*(2), 101–109.

DeCarlo, P. F., Slowik, J. G., Worsnop, D. R., Davidovits, P., & Jimenez, J. L. (2004). Particle morphology and density characterization by combined mobility and aerodynamic diameter measurements. Part 1: Theory. *Aerosol Science and Technology*, *38*(12), 1185–1205.

Delhaye, D., Ouf, F.-X., Ferry, D., Ortega, I. K., Penanhoat, O., Peillon, S., … Irimiea, C. (2017). The MERMOSE project: Characterization of particulate matter emissions of a commercial aircraft engine. *Journal of Aerosol Science*, *105*, 48–63.

Dobbins, R. A., Mulholland, G. W., & Bryner, N. P. (1994). Comparison of a fractal smoke optics model with light extinction measurements. *Atmospheric Environment*, *28*(5), 889–897.

Döpelheuer, A. (2002). No Title. *Anwendungsorientierte Verfahren Zur Bestimmung von CO, HC Und Ruß Aus Luftfahrttriebwerken*.

Durdina, L., Brem, B. T., Abegglen, M., Lobo, P., Rindlisbacher, T., Thomson, K. A., … Wang, J. (2014). Determination of PM mass emissions from an aircraft turbine engine using particle effective density. *Atmospheric Environment*, *99*, 500–507.

Eggersdorfer, M. L., Gröhn, A. J., Sorensen, C. M., McMurry, P. H., & Pratsinis, S. E. (2012a). Mass-mobility characterization of flame-made ZrO 2 aerosols: Primary particle diameter and extent of aggregation. *Journal of Colloid and Interface Science*, *387*(1), 12–23.

Eggersdorfer, M. L., Kadau, D., Herrmann, H. J., & Pratsinis, S. E. (2012b). Aggregate morphology evolution by sintering: number and diameter of primary particles. *Journal of Aerosol Science*, *46*, 7–19.

Eggersdorfer, M. L., & Pratsinis, S. E. (2012). The structure of agglomerates consisting of polydisperse particles. *Aerosol Science and Technology*, *46*(3), 347–353.

Ghazi, R., Tjong, H., Soewono, A., Rogak, S. N., & Olfert, J. S. (2013). Mass, mobility, volatility, and morphology of soot particles generated by a McKenna and inverted burner. *Aerosol Science and Technology*, *47*(4), 395–405.

Giechaskiel, B., Chirico, R., DeCarlo, P. F., Clairotte, M., Adam, T., Martini, G., … Astorga, C. (2010). Evaluation of the particle measurement programme (PMP) protocol to remove the vehicles' exhaust aerosol volatile phase. *Science of The Total Environment*, *408*(21), 5106–5116. https://doi.org/10.1016/J.SCITOTENV.2010.07.010

Giechaskiel, B., Maricq, M., Ntziachristos, L., Dardiotis, C., Wang, X., Axmann, H., … Schindler, W. (2014). Review of motor vehicle particulate emissions sampling and measurement: From smoke and filter mass to particle number. *Journal of Aerosol Science*, *67*, 48–86.

Goldberg, E. (1985). Black Carbon in the Environment. *Wiley and Sons,New York, NY*. Retrieved from https://www.osti.gov/scitech/biblio/5473087

Good, N., Mölter, A., Peel, J. L., & Volckens, J. (2017). An accurate filter loading correction is essential for assessing personal exposure to black carbon using an Aethalometer. *Journal of Exposure Science and Environmental Epidemiology*, *27*(4), 409.

Graves, B. (2019). E-mail to Brian Graves on the particle loss corrections that were applied to the CIDI Dataset in Graves et al. (2015).

Graves, B., Olfert, J., Patychuk, B., Dastanpour, R., & Rogak, S. (2015). Characterization of particulate matter morphology and volatility from a compression-ignition natural-gas direct-injection engine. *Aerosol Science and Technology*, *49*(8), 589–598.

Hinds, W. C. (1999). Aerosol Technology: Properties. *Behavior, and Measurement of Airborne Particles (2nd*.

ICAO. (2016). *2016 Environmental Report - On Board A Sustainable Future*. Montreal, Canada: International Civil Aviation Organization (ICAO). Retrieved from http://www.icao.int/environmental-protection/Documents/ICAO Environmental Report 2016.pdf

Janssen, N. A., Hoek, G., Simic-Lawson, M., Fischer, P., van Bree, L., ten Brink, H., … Cassee, F. R. (2011). Black carbon as an additional indicator of the adverse health effects of airborne particles compared with PM10 and PM2.5. *Environmental Health Perspectives*, *119*(12), 1691–1699. https://doi.org/10.1289/ehp.1003369 [doi]

Jeßberger, P., Voigt, C., Schumann, U., Sölch, I., Schlager, H., Kaufmann, S., … Gayet, J.-F. (2013). Aircraft type influence on contrail properties. *Atmospheric Chemistry and Physics*, *13*(23), 11965–11984.

Johnson, T. J., Olfert, J. S., Symonds, J. P. R., Johnson, M., Rindlisbacher, T., Swanson, J. J., … Walters, D. (2015). Effective density and mass-mobility exponent of aircraft turbine particulate matter. *Journal of Propulsion and Power*, *31*(2), 573–582.

Johnson, T. J., Symonds, J. P. R., & Olfert, J. S. (2013). Mass–mobility measurements using a centrifugal particle mass analyzer and differential mobility spectrometer. *Aerosol Science and Technology*, *47*(11), 1215–1225.

Kärcher, B., & Yu, F. (2009). Role of aircraft soot emissions in contrail formation. *Geophysical Research Letters*, *36*(1).

Kinney, P. D., Pui, D. Y. H., Mulliolland, G. W., & Bryner, N. P. (1991). Use of the electrostatic classification method to size 0.1 µm SRM particles—a feasibility study. *Journal of Research of the National Institute of Standards and Technology*, *96*(2), 147.

Kittelson, D. B. (1998). Engines and nanoparticles: a review. *Journal of Aerosol Science*, *29*(5–6), 575–588.

Korolev, A., Emery, E., & Creelman, K. (2013). Modification and tests of particle probe tips to mitigate effects of ice shattering. *Journal of Atmospheric and Oceanic Technology*, *30*(4), 690–708.

Kreyling, W. G., Semmler-Behnke, M., & Möller, W. (2006). Ultrafine particle–lung interactions: does size matter? *Journal of Aerosol Medicine*, *19*(1), 74–83.

Laden, F., Schwartz, J., Speizer, F. E., & Dockery, D. W. (2006). Reduction in fine particulate air pollution and mortality: extended follow-up of the Harvard Six Cities study. *American Journal of Respiratory and Critical Care Medicine*, *173*(6), 667–672.

Lee, D. S., Pitari, G., Grewe, V., Gierens, K., Penner, J. E., Petzold, A., … Berntsen, T. (2010). Transport impacts on atmosphere and climate: Aviation. *Atmospheric Environment*, *44*(37), 4678–4734.

Liati, A., Brem, B. T., Durdina, L., Vögtli, M., Arroyo Rojas Dasilva, Y., Dimopoulos Eggenschwiler, P., & Wang, J. (2014). Electron microscopic study of soot particulate matter emissions from aircraft turbine engines. *Environmental Science & Technology*, *48*(18), 10975–10983.

Liu, Z. G., Vasys, V. N., Dettmann, M. E., Schauer, J. J., Kittelson, D. B., & Swanson, J. (2009). Comparison of strategies for the measurement of mass emissions from diesel engines emitting ultra-low levels of particulate matter. *Aerosol Science and Technology*, *43*(11), 1142–1152.

Lobo, P., Durdina, L., Smallwood, G. J., Rindlisbacher, T., Siegerist, F., Black, E. A., … Miake-Lye, R. C. (2015a). Measurement of aircraft engine non-volatile PM emissions: Results of the aviation-particle regulatory instrumentation demonstration experiment (A-PRIDE) 4 campaign. *Aerosol Science and Technology*, *49*(7), 472–484.

Lobo, P., Hagen, D. E., Whitefield, P. D., & Raper, D. (2015b). PM emissions measurements of in-service commercial aircraft engines during the Delta-Atlanta Hartsfield Study. *Atmospheric Environment*, *104*, 237–245.

Martini, G., Giechaskiel, B., & Dilara, P. (2009). Future European emission standards for vehicles: the importance of the UN-ECE Particle Measurement Programme. *Biomarkers*, *14*(sup1), 29–33.

McMurry, P. H., Wang, X., Park, K., & Ehara, K. (2002). The relationship between mass and mobility for atmospheric particles: A new technique for measuring particle density. *Aerosol Science & Technology*, *36*(2), 227–238.

Moore, R. H., Thornhill, K. L., Weinzierl, B., Sauer, D., D'Ascoli, E., Kim, J., … Beyersdorf, A. J. (2017). Biofuel blending reduces particle emissions from aircraft engines at cruise conditions. *Nature*, *543*(7645), 411–415.

Moran, J., Cuevas, J., Liu, F., Yon, J., & Fuentes, A. (2018). Influence of primary particle polydispersity and overlapping on soot morphological parameters derived from numerical TEM images. *Powder Technology*, *330*, 67–79.

Oh, C., & Sorensen, C. M. (1997). The Effect of Overlap between Monomers on the Determination of Fractal Cluster Morphology. *Journal of Colloid and Interface Science*, *193*(1), 17–25. https://doi.org/10.1006/JCIS.1997.5046

Olfert, J. S., Dickau, M., Momenimovahed, A., Saffaripour, M., Thomson, K., Smallwood, G., … Crayford, A. (2017). Effective density and volatility of particles sampled from a helicopter gas turbine engine. *Aerosol Science and Technology*, *51*(6), 704–714.

Owen, M., Mulholland, G., & Guthrie, W. (2012). Condensation Particle Counter Proportionality Calibration from 1 particle· cm− 3 to 104 particles· cm− 3. *Aerosol Science and Technology*, *46*(4), 444–450.

Park, K., Kittelson, D. B., & McMurry, P. H. (2004). Structural properties of diesel exhaust particles measured by transmission electron microscopy (TEM): Relationships to particle mass and mobility. *Aerosol Science and Technology*, *38*(9), 881–889.

Park, K., Kittelson, D. B., Zachariah, M. R., & McMurry, P. H. (2004). Measurement of inherent material density of nanoparticle agglomerates. *Journal of Nanoparticle Research*, *6*(2), 267–272.

Peck, J., Oluwole, O. O., Wong, H.-W., & Miake-Lye, R. C. (2013). An algorithm to estimate aircraft cruise black carbon emissions for use in developing a cruise emissions inventory. *Journal of the Air & Waste Management Association*, *63*(3), 367–375.

Penner, J., Lister, D., Griggs, D., Dokken, D., & McFarland, M. (1999). *Summary for Policymakers - Aviation and the Global Atmosphere*. Intergovernmental Panel on Climate Change (IPCC). Retrieved from https://www.ipcc.ch/pdf/special-reports/spm/av-en.pdf

Peters, A., Rückerl, R., & Cyrys, J. (2011). Lessons From Air Pollution Epidemiology for Studies of Engineered Nanomaterials. *Journal of Occupational and Environmental Medicine*, *53*, S8–S13. https://doi.org/10.1097/JOM.0b013e31821ad5c0

Peters, C. A. (2001). Statistics for analysis of experimental data. *Environmental Engineering Processes Laboratory Manual*, 1–25.

Petzold, A., Döpelheuer, A., Brock, C. A., & Schröder, F. (1999). In situ observations and model calculations of black carbon emission by aircraft at cruise altitude. *Journal of Geophysical Research: Atmospheres*, *104*(D18), 22171–22181.

Petzold, A., Ogren, J. A., Fiebig, M., Laj, P., Li, S.-M., Baltensperger, U., … Sugimoto, N. (2013). Recommendations for reporting" black carbon" measurements. *Atmospheric Chemistry and Physics*, *13*(16), 8365–8379.

Pope III, C. A., & Dockery, D. W. (2006). Health effects of fine particulate air pollution: lines that connect. *Journal of the Air & Waste Management Association*, *56*(6), 709–742.

Rogak, S. (2019). E-mail to Steve Rogak on the Equation linking the BC primary particle diameter to the mobility diameter.

Rogak, S. N., Flagan, R. C., & Nguyen, H. V. (1993). The mobility and structure of aerosol agglomerates. *Aerosol Science and Technology*, *18*(1), 25–47.

Rogak, S. N., & Olfert, J. S. (2019). (In Press) Universal relations between soot effective density and primary particle size for common combustion sources. *Aerosol Science & Technology*.

Saltelli, A., Ratto, M., Andres, T., Campolongo, F., Cariboni, J., Gatelli, D., … Tarantola, S. (2008). *Global sensitivity analysis: the primer*. John Wiley & Sons.

Samset, B. H., Myhre, G., Herber, A., Kondo, Y., Li, S.-M., Moteki, N., … Balkanski, Y. (2014). Modelled black carbon radiative forcing and atmospheric lifetime in AeroCom Phase II constrained by aircraft observations. *Atmospheric Chemistry and Physics*, *14*(22), 12465–12477.

Schmid, O., & Stoeger, T. (2016). Surface area is the biologically most effective dose metric for acute nanoparticle toxicity in the lung. *Journal of Aerosol Science*, *99*, 133–143.

Schumann, U. (2012). A contrail cirrus prediction model. *Geoscientific Model Development*, *5*, 543–580.

Schumann, U., Jeßberger, P., & Voigt, C. (2013). Contrail ice particles in aircraft wakes and their climatic importance. *Geophysical Research Letters*, *40*(11), 2867–2872.

Sorensen, C. M. (2011). The mobility of fractal aggregates: a review. *Aerosol Science and Technology*, *45*(7), 765–779.

Steiner, S., Bisig, C., Petri-Fink, A., & Rothen-Rutishauser, B. (2016). Diesel exhaust: current knowledge of adverse effects and underlying cellular mechanisms. *Archives of Toxicology*, *90*(7), 1541–1553.

Stettler, M. E. J., Boies, A., Petzold, A., & Barrett, S. R. H. (2013a). Global civil aviation black carbon emissions. *Environmental Science & Technology*, *47*(18), 10397–10404.

Stettler, M. E. J., Swanson, J. J., Barrett, S. R. H., & Boies, A. M. (2013b). Updated correlation between aircraft smoke number and black carbon concentration. *Aerosol Science and Technology*, *47*(11), 1205–1214.

UNECE. (2010). *Uniform Provisions Concerning the Approval of Vehicles with Regard to the Emission of Pollutants According to Engine Fuel Requirements.* Retrieved from https://publications.europa.eu/en/publication-detail/-/publication/2f8f0ce5-66fb-4a38-ae68-558ae1b04a5f/language-en

Vander Wal, R. L., Bryg, V. M., & Huang, C.-H. (2014). Aircraft engine particulate matter: Macro-micro-and nanostructure by HRTEM and chemistry by XPS. *Combustion and Flame*, *161*(2), 602–611.

Wang, C. (2004). A modeling study on the climate impacts of black carbon aerosols. *Journal of Geophysical Research: Atmospheres*, *109*(D3).

Wentzel, M., Gorzawski, H., Naumann, K.-H., Saathoff, H., & Weinbruch, S. (2003). Transmission electron microscopical and aerosol dynamical characterization of soot aerosols. *Journal of Aerosol Science*, *34*(10), 1347–1370.

Wey, C. C., Anderson, B. E., Hudgins, C., Wey, C., Li-Jones, X., Winstead, E., … Whitefield, P. (2006). Aircraft particle emissions experiment (APEX).

Wiedensohler, A., Wiesner, A., Weinhold, K., Birmili, W., Hermann, M., Merkel, M., … Tuch, T. (2018). Mobility particle size spectrometers: Calibration procedures and measurement uncertainties. *Aerosol Science and Technology*, *52*(2), 146–164.

Williams, J., Reus, M. de, Krejci, R., Fischer, H., & Ström, J. (2002). Application of the variability-size relationship to atmospheric aerosol studies: estimating aerosol lifetimes and ages. *Atmospheric Chemistry and Physics*, *2*(2), 133–145.

Zhou, C., & Penner, J. E. (2014). Aircraft soot indirect effect on large-scale cirrus clouds: Is the indirect forcing by aircraft soot positive or negative? *Journal of Geophysical Research: Atmospheres*, *119*(19).